Chemical Science

ROYAL SOCIETY OF CHEMISTRY

EDGE ARTICLE

View Article Online
View Journal | View Issue

Cite this: *Chem. Sci.*, 2021, **12**, 5664

All publication charges for this article have been paid for by the Royal Society of Chemistry

Received 26th November 2020
Accepted 6th March 2021

DOI: 10.1039/d0sc06502a

rsc.li/chemical-science

The dome of gold nanolized for catalysis†

Yao Peng, Cheng Shang * and Zhi-Pan Liu *

Gold is noble in bulk but turns out to be a superior catalyst at the nanoscale when supported on oxides, in particular titania. The critical thickness for activity, namely two-layer gold particles on titania, observed two decades ago represents one of the most influential mysteries in the recent history of heterogeneous catalysis. By developing a Bayesian optimization controlled global potential energy surface exploration tool with machine learning potential, here we determine the atomic structures of gold particles within ~2 nm on a TiO_2 surface. We show that the smallest stable Au nanoparticle is Au_{24} which is pinned on the oxygen-rich TiO_2 and exhibits an unprecedented dome architecture made by a single-layer Au sheet but with an apparent two-atomic-layer height. Importantly, this has the highest activity for CO oxidation at room temperature. The physical origin of the high activity is the outstanding electron storage ability of the nano-dome, which activates the lattice oxygen of the oxide. The determined CO oxidation mechanism, the simulated rate and the fitted apparent energy barrier are consistent with known experimental facts, providing key evidence for the presence of both the high-activity Au dome and the low-activity close-packed Au particles in real catalysts. The future direction for the preparation of active and stable Au-based catalysts is thus outlined.

1. Introduction

Metal and metal oxide composites represent a classical type of heterogeneous catalyst, renowned for complex multi-element nanostructures at interfaces.[1–4] Knowledge about the active sites of these catalysts, although of great significance to industry, is however largely speculative due to the lack of efficient tools to map out atoms at interfaces.[5–7] Experimental studies face great challenges in achieving high local resolution of both geometry and electronic structures,[8] whilst theory generally fails to give either high speed or high accuracy in exploring the potential energy surface (PES) of interfaces.[9] Here we show that the latest machine learning (ML)-based atomic simulation can resolve the atomic structure of gold nanoparticles on TiO_2 in low temperature CO oxidation, a well-known but puzzling example used to illustrate the phenomenological synergetic effect of composites in catalysis.[10–12] By meticulously scanning gold particles with subnano to ~2 nm in dimension, we identify a unique gold nano-dome of 0.62 nm in height anchored on oxygen-rich TiO_2, which is not only the smallest stable particle but also the most active for low temperature CO oxidation.

Oxide-supported Au catalysts exhibit attractive low temperature (down to 200 K) CO oxidation activity.[13,14] Since the first report of Au/TiO_2 by Haruta *et al.* in the 1980s,[14,15] a large volume of literature, encompassing both experimental and theoretical studies, has been devoted to understanding its physical properties, focusing on the active site and the mechanism.[16–22] Goodman's group laid a milestone for understanding the Au/TiO_2 composite system,[10] using surface science techniques to establish that the most active Au particles are nano-sized and have a two-layer height (0.7 nm). However, Emmanuel *et al.* recently used a model catalyst experiment and only found an exponential activity increase with a reduction of particle diameter from 6 to 1.5 nm; there was no abrupt activity jump at a certain particle size.[23] Indeed, because supported particles generally have a wide size distribution, it has not been possible to either confirm the critical thickness for activity or identify the true active site in supported gold catalysts.

Apart from the structural uncertainty, the CO oxidation mechanism is highly controversial, with uncertainty over whether or not the reaction follows the Mars–van Krevelen (M–vK) mechanism[24] in which the lattice O of oxide takes part in CO oxidation. A recent experiment by Behm and co-workers showed the participation of atomic O (stable up to 353 K) in CO oxidation,[25,26] indicating the dissociative adsorption of molecular O_2. However, the atomic O from O_2 may well become the interfacial O between Au and TiO_2 (an interface Langmuir–Hinshelwood (LH) mechanism), rather than forming the lattice O, and thus there is no conclusive evidence for the occurrence of the M–vK mechanism. On the other hand, the past two decades have witnessed a large volume of theoretical studies using different

Collaborative Innovation Center of Chemistry for Energy Material, Shanghai Key Laboratory of Molecular Catalysis and Innovative Materials, Key Laboratory of Computational Physical Science, Department of Chemistry, Fudan University, Shanghai 200433, China. E-mail: cshang@fudan.edu.cn; zpliu@fudan.edu.cn

† Electronic supplementary information (ESI) available: Supplementary methods; the global minima of other Au_nO_m/TiO_2 particles; training dataset and benchmark of the G-NN potential. See DOI: 10.1039/d0sc06502a

models for Au/TiO_2 [27–31] and the computed data for activity appears diverse. The CO oxidation barrier is reported to be 0.3 eV on Au_{18}/TiO_2 (110) with an LH mechanism,[27,28] but it jumps to 0.8 eV for a supported Au_{20} particle with a M–vK mechanism.[29,30] In contrast, using periodic Au stripe models on TiO_2, the barrier turns out to be ~0.5 eV where O_2 dissociation is the rate determining factor.[32,33] Since there is no quantitative consensus for the activity reported from different hypothetical models, the key to these puzzles boils down to the "true" atomic structure of the gold nanoparticles on TiO_2 under the reaction conditions.

Recent years have seen an increasing number of atomic simulation applications with ML potential for structure determination.[34–37] The applications are, however, generally limited to relatively simple systems (*e.g.* bulk with few elements) due to the great difficulty in generating reliable multiple-element potentials for structure prediction, which requires the good description of the global PES.[38] Here a Bayesian-guided global optimization tool is developed to advance the simulation of complex catalytic reactions under realistic conditions, with the aim of efficient structure determination of a multi-element composite. The method utilizes a Bayesian optimization algorithm[39] to guide the ML-based global PES search,[40–43] in which the stochastic surface walking (SSW)[40,41] global optimization with global neural network (G-NN) potential acts as the key tool for ML potential construction and global PES exploration.[44–47] Using this Bayesian-guided SSW-NN search, we managed to reveal the global minima (GM) of gold particles up to Au_{52} on reduced, stoichiometric and oxidized TiO_2 (110) surfaces. The smallest stable Au cluster, *i.e.* an $Au_{24}O_4$ dome made by a single-layer Au sheet but with an apparent two-atomic-layer height, is identified as the key component for catalyzing low temperature CO oxidation.

2. Methods and calculation details

2.1. Bayesian-guided SSW-NN simulation

The GM of all gold particles was obtained using our recently-developed SSW-NN method as implemented in LASP code (http://www.lasphub.com),[48] in which the SSW-NN achieves fast global PES exploration. Fig. 1a illustrates two key steps for Bayesian-guided SSW-NN simulation. First the ML potential (the G-NN potential) is generated by the standard SSW-NN process *via* the iterative self-learning of the plane-wave density functional theory (DFT) global PES dataset generated from SSW exploration. There are three steps: (i) global dataset generation based on DFT calculations using selected structures from SSW simulation from random bulk and slab structures, (ii) G-NN potential fitting and (iii) SSW global optimization using the G-NN potential. These three steps are iteratively performed until the G-NN potential is transferable and robust enough to describe the global PES.

Second, Bayesian optimization is utilized to drive the iterative acquisition-surrogate procedure, *i.e.* predicting new GM structures by SSW-NN searches and updating the G-NN potential by learning thse GM structures. Bayesian optimization is terminated when the GM predicted from SSW-NN is confirmed after more than 5 Bayesian cycles. The procedure is standardized in LASP as described recently by Ma *et al.*[49]

We should emphasize that the structures that were iteratively added into the dataset during the G-NN potential generation, were always selected from SSW global optimization trajectories according to the structure and energy criteria. These structures either have distinct local structure as reflected by structure descriptors, or have a large energy deviation between NN and DFT results. To generate the AuTiO potential, we obtained 44 096 structures after the standard SSW-NN procedure, and we further added 418 AuO_x/TiO_2 structures, including 187 $Au_{24}O_x/TiO_2$ structures, into the final stage of Bayesian optimization to search for AuO_x particles on TiO_2. The AuTiCO global dataset consisted of 54 127 structures, including 53 582 from the standard SSW-NN procedure, and 545 from Bayesian optimization. All structures in the dataset were calculated by plane–wave DFT calculation with average setups (also see Section 2.2 for details). The input files of these calculations to reproduce the training set can be found on the lasphub website.[50] The AuTiO G-NN potential has a four-layer (198-50-50-1) feed-forward NN structure, with a total of 37 753 fitting parameters. The root-mean-square (RMS) errors for the energy and the force of the G-NN are 6.3 meV per atom and 0.155 eV $Å^{-1}$, respectively (see ESI† part 3 for more details).

2.2. DFT calculations

All DFT calculations were performed by using plane-wave DFT code, VASP,[51,52] in which the electron–ion interaction is represented by the projector augmented wave (PAW) pseudopotential.[51] The kinetic energy cutoff was 450 eV. The exchange functional GGA-PBE[53] was used for training dataset generation. The CO oxidation mechanism exploration and the analyses of the projected density of states (p-DOS) and Bader charge were carried out using the spin-polarized GGA-PBE with the local Hubbard term U correction (PBE + U) (U = 5 eV) for the Ti 3d orbital.[54] The dispersion effect on reactions was examined by using Grimme's D3 correction (PBE-D3)[55] (see ESI, Table S4†), which shows that the inclusion of dispersion does not change the CO oxidation kinetics. The first Brillouin zone k-point sampling utilized the Monkhorst–Pack scheme with an automated mesh determined by 25 times the reciprocal lattice vectors for bulk, and only the Γ point for surface in the slab model [a large unit cell of 26.7 Å × 19.7 Å, corresponding to the $p(9 \times 3)$ rutile (110) surface]. The energy and force criteria for convergence of the electron density and structure optimization were set at 10^{-5} eV and 0.01 eV $Å^{-1}$, respectively. All the transition states (TS) were located using the double-ended surface walking method (DESW).[56]

3. Results and discussions

3.1. Structure of supported Au particles

To map out the active site responsible for CO oxidation, we investigated a series of gold particles on titania, namely Au_nO_m/TiO_2 (illustrated in Fig. 1b) with Bayesian-guided SSW-NN, with each composition (by varying n and m) being visited by more

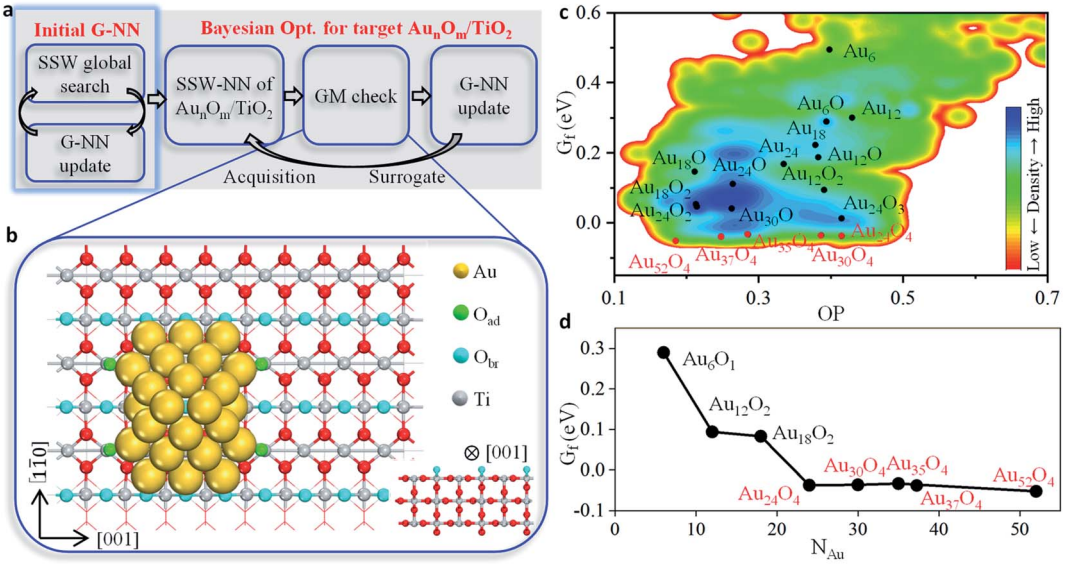

Fig. 1 Au_nO_m/TiO_2 structure determination using Au–Ti–O G-NN potential-based global optimization. (a) Illustration of the Bayesian-SSW-NN methodology for identifying the GM of Au_nO_m/TiO_2. (b) Example of Au_nO_m/TiO_2 utilized in the Bayesian-SSW-NN search. TiO_2 is represented by a $p(9 \times 3)$ $TiO_2(110)$ surface (the side view is inset). (c) Global PES contour plot of Au_nO_m/TiO_2 systems containing 3×10^5 low energy minima from SSW-NN. The x axis is a distance-weighted Steinhart order parameter (OP), the y axis is the free formation energy (G_f) of Au_nO_m and the color indicates the density of states for the minima. The GM of representative clusters are labelled in the map as black and red dots. (d) G_f of the GM of Au_nO_m/TiO_2 (n = 6, 12, 18, 24, 30, 35, 37 and 52).

than 10^5 minima. The numbers of Au atoms ("n" of Au_nO_m) studied in this work were 6, 12, 17, 18, 20, 22, 24, 30, 31, 32, 35, 36, 37 and 52, and here only the most representative examples are reported in Fig. 1b for clarity. TiO_2 was modelled as rutile TiO_2 (110) with up to $p(9 \times 3)$ surface area, as illustrated in Fig. 1b. This corresponds to Au exposure from 8% to 71% ML (1 ML is 1.387×10^{15} Au atoms per cm^2 corresponding to Au (111)). The shortest distance between adjacent Au particles was at least 9.38 Å (occurred in the largest $Au_{52}O_4$ particle), which is large enough to avoid lateral interactions between particles. The formal oxidation state of Au in Au_nO_m particles was subject to the O_2 chemical potential (see ESI Table S1†) and thus the amount of O (m value) in the simulation varied from −1 to 5 (−1 indicates an O vacancy near Au). The free formation energy of Au_nO_m, G_f (eV per Au atom), could be determined by reference to the TiO_2 stoichiometric surface, Au (111) surface and O_2 at ambient conditions (eqn (S1) and (S2) in ESI†). In computing the free energy, we utilized the DFT total energy to approximate the free energy for solid states (AuO_x/TiO_2, TiO_2) because the vibration entropy and the pV term contributions of solid phases are negligibly small; and we corrected the zero-point-energy, thermal and entropy contributions for gas phase O_2 molecule at finite temperatures.[57] While all structure candidates were obtained from SSW-NN, the low energy structures were always checked by DFT to achieve high accuracy, and all key energetics reported in this work are DFT results.

In Fig. 1c, we show the global PES contour map of Au_nO_m/TiO_2 by plotting G_f against a distance-weighted Steinhart order parameter[58,59] (OP) of all low energy minima. The smaller the OP value is, the more close-packed the Au particles will be. Fig. 1c shows clearly that the larger particles have lower G_f, indicating the sintering tendency of very small-sized particles (<20 atoms), as also observed in experiments.[10,11] We note that the bare Au particles on the stoichiometric surface and the reduced surface (with oxygen vacancies) are the least stable. As shown in ESI Fig. S1,† the GMs of Au_nO_{-1}/TiO_2 and Au_n/TiO_2 (n = 12, 18 and 24) adopt the close-packed stick configuration. The stick grows in the groove between two protruding rows of bridge O (O_{br}) on $TiO_2(110)$ along [1$\bar{1}$0], interacting with the surface *via* eight Au–O_{br} bonds. For Au_nO_{-1}/TiO_2, the Au particles prefer to sit away from the surface O_{br} vacancies, which is consistent with the previous experimental observation.[11] Importantly, the presence of additional O, *i.e.* forming O-containing Au_nO_m particles (m > 1), not only stabilizes the particles, but also largely smoothens the G_f difference between particles. From Au_{18} to Au_{24}, G_f drops by 0.05 eV, and it changes by only 0.007 eV from $Au_{18}O_2$ to $Au_{24}O_2$. In the bottom of the global PES, we identify $Au_{24}O_4$ and $Au_{52}O_4$, which are the two most stable particles with G_f values of −0.04 and −0.05 eV per Au, respectively. Our results indicate that subnano and nano Au particles can resist sintering (G_f < 0) as long as the TiO_2 surface is O-rich, which is indeed possible under oxidation conditions.[11] The thermodynamic stability of these particles is summarized in Fig. 1d for each size. We can see that with increasing particle size, more O atoms are required to stablize the particle. In all cases, these extra O near to Au (O_{ad}) reside on the exposed five-coordinated Ti site (Ti_{5c}, see Fig. 1b) at the Au/TiO_2 interface, acting as the anchor to stabilize Au particles. In the following, we describe the GMs for three representative sizes.

Au_6O in Fig. 2 has a structure typical of Au particles below 20 atoms, and is highly unstable with a G_f value of +0.3 eV. It grows in the groove between two protruding rows of bridge O (O_{br}) on

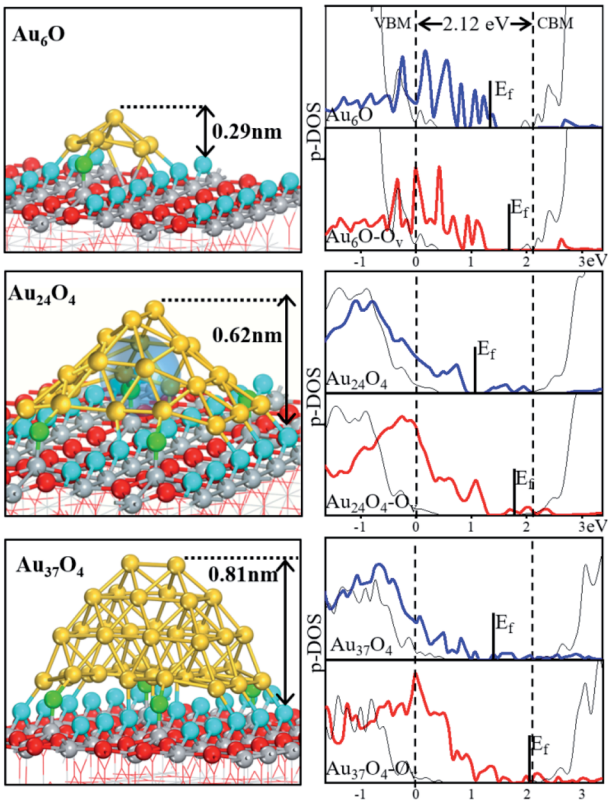

Fig. 2 Geometrical structures and p-DOS of Au_nO_m/TiO_2. Geometrical structures of Au_6O, $Au_{24}O_4$ and $Au_{37}O_4$ on TiO_2 (110) (left panel) and the corresponding p-DOS for the 5d (Au) before (blue) and after (red) the formation of a surface O vacancy (right panel). All the DOSs are aligned *via* the Ti 3d states of the bulk TiO_2. E_f indicates the Fermi level; the black lines represent the total DOS of bulk TiO_2; the vertical dot lines indicate the valence band minimum (VBM) and CBM of bulk TiO_2, respectively. The colour scheme of atoms is the same as that used in Fig. 1b, and the transparent ball represents the void space.

TiO_2 (110) along [1$\bar{1}$0], anchored to the surface *via* Au–O_{br} bonds.[10,60] The particle is a single-layer thick, but the Au atoms not linked with O_{br} are higher in position. The Au_6O particle is 0.30 nm high and 0.44 nm in diameter. The Au coordination number (CN, Au–Au coordination shell) is very low, being only 4.25 on average (*c.f.* CN = 9 for Au in the Au (111) surface).

Turning to Au_{24}, the particle can hold four additional O_{ad} atoms at the perimeter sites, *i.e.* $Au_{24}O_4$, and is thus much stabilized. The particle expands to cover three O_{br} rows, and the Au atoms form one highly curved two-dimensional sheet. Interestingly, the particle has a dome architecture with C_{2v} symmetry and a large hollow void in between the Au sheet and TiO_2 (see the transparent ball in Fig. 2). It reaches 0.62 nm in height and spans 1.16 nm in diameter. Due to its single-layer nature, the Au atoms still have low coordination numbers (CN = 4.7 on average) and thus locate at the bottom-right corner in the Fig. 1c global PES. We note that structures in this region (*i.e.* OP > 0.41) all have the dome structure, clearly different from close-packing configurations (OP < 0.2).

Further increasing the Au coverage gives Au particles that are not only thicker but also more close-packed. At Au_{37}, the GM is $Au_{37}O_4$, which is 0.81 nm high but still 1.16 nm in diameter. Compared to $Au_{24}O_4$, the additional Au atoms fill in the void of the dome by first sealing the bottom to form a close-packed Au layer base ($Au_{35}O_4$, ESI Fig. S2†) and then occupying the middle cavity until $Au_{37}O_4$ forms (Fig. 2). By further increasing Au atoms, $Au_{52}O_4$ is eventually formed (ESI Fig. S2†), which is 1.3 nm in diameter and 1.01 nm in height, having a similar stability to $Au_{24}O_4$. Both $Au_{37}O_4$ and $Au_{52}O_4$ are fcc close-packed Au pyramids in which the average CN of Au in $Au_{52}O_4$ is 6.9, close to that for Au in the Au (111) surface (CN = 9).

3.2. Electronic structure of supported Au particles

The O-rich TiO_2 surface not only helps to stabilize Au particles but also influences the nearby lattice O stability. We have computed the energy required to create one O vacancy (E_{Ov}) by removing the O_{br} nearest to the Au particles (ESI Table S2†). For small particles, *e.g.* Au_6O to $Au_{18}O_2$, E_{Ov} remains similar to or is even higher than that for bare TiO_2 (110) (2.36 eV). However, for the larger particles, *i.e.* $Au_{24}O_4$ and $Au_{35}O_4$, E_{Ov} reduces significantly to 1.66 eV and then it increases to 2.08 eV for $Au_{37}O_4$ and 2.21 eV for $Au_{52}O_4$. These results indicate that this O_{br} atom is significantly activated only when the Au particle is larger than 1 nm, especially when the void is present. Because the lattice O_{br} is a negatively charged anion, the creation of O_v on the TiO_2 surface leads to the emergence of high energy electrons near O_v.[11] The low-lying unoccupied states in Au, if present, should help to stabilize the O_v, through electron transfer from the surface to Au. Indeed, our Bader charge analyses confirm a significant charge transfer for Au_{24} and Au_{35} systems, much more than is found for Au_6: the entire particle gains 0.02, 0.65 and 0.54*e* after O_v formation for Au_6O, $Au_{24}O_4$ and $Au_{37}O_4$, respectively. To provide deeper insights, we therefore considered the electronic structures. In Fig. 2 (right panel), we have plotted the p-DOSs for the Au 5d states in three representative systems (Au_6O, $Au_{24}O_4$ and $Au_{37}O_4$ on TiO_2), both before and after the formation of a surface O vacancy, namely Au_nO_m and Au_nO_m–O_v. These p-DOSs (5d) reflect the different responses of the Au particles in creating O_v, as described below.

In Au_6O/TiO_2, most Au 5d states are occupied and the remaining antibonding 5d states are far above the conduction band minimum (CBM) of TiO_2. The Fermi level states are related to the delocalized bonding between Au and O_{br}. After the O_{br} removal, these Au 5d states diminish, indicating that the creation of O_v is at the cost of the Au–O_{br} interaction.

In $Au_{24}O_4/TiO_2$ and $Au_{37}O_4/TiO_2$, a significant number of low-lying unoccupied Au 5d states are present, *i.e.* below the CBM, before O_v creation, suggesting their capacity to store extra electrons. After O_{br} removal, there is an up-shift of the Fermi level that crosses the continuous Au 5d states in both systems. Obviously, this is the consequence of electron transfer from the oxide surface to Au, leading to electron accumulation on the Au 5d states. For $Au_{37}O_4$, the highest occupied molecular orbital (HOMO) of Au is relatively high, which is due to the fact that the close-packed morphology is similar to that of the bulk structure, and thus reduces the ability of the Au particles to receive electrons. Such results are consistent with the experimental

observation that Au particles start to exhibit metallicity when the height is 0.6–1 nm.[61] We note that these unoccupied 5d states of $Au_{24}O_4$ have aromatic bonding characteristics, exhibiting a highly delocalized nature throughout the whole particle (ESI Fig. S3†). They are similar to those in the stand-alone Au_{32} hollow cage, which also has aromatic 5d states (ESI Fig. S4†). Apparently, the delocalized 5d bonding is the key to stabilizing the dome structure, which is favored over the close-packed configuration in small Au particles (Au_{24}, Au_{30} and Au_{37} investigated in this work).

3.3. CO oxidation reaction

With the elucidation of the atomic structure of supported Au particles, we are now at the position to explore CO oxidation activity. We constructed a four-element G-NN potential, Au–Ti–C–O, based on the dataset of the Au–Ti–O potential, to which a number of structure configurations for CO adsorption and CO oxidation in the AuTiO system were added from the self-learning SSW reaction sampling data. Because we limited the reaction to the CO oxidation at the Au–TiO_2 interface, the training of the four-element potential was relatively facile, but it is tremendously helpful for exploring the possible CO oxidation channels. The detail of the construction of the AuTiCO potential can be found in the ESI.† Considering that the supported Au particles need to be sufficiently thermodynamically stable during catalysis, we focused on reactions on $Au_{24}O_4$ and $Au_{37}O_4$. $Au_{24}O_4$ is the smallest stable particle with void morphology while $Au_{37}O_4$ is the smallest close-packed structure representative of the larger fcc particles in general. The dynamic stability of these particles at finite temperatures was examined and is discussed later. Since CO oxidation occurs under an O_2 atmosphere and thus the supply of interfacial O is guaranteed, the surface O vacancies should be filled readily during the steady state conversion.

Utilizing the G-NN potential, we were able to explore all the likely reaction pathways on the supported catalysts, and the lowest energy pathways identified from the G-NN simulation were then confirmed by DFT calculations. The reaction mechanisms on the two supported Au particle types were found to be similar, both following the M–vK mechanism in which the lattice oxygen at the surface takes part in reacting with CO molecules to form CO_2. Overall, the reaction can be divided into four key elementary steps:

(i) $CO^* + O_{br} \rightarrow CO_2 + O_v$. An adsorbed CO (CO*) on interfacial Au reacts with the nearby lattice O_{br}.

(ii) $O_v + O_2 \rightarrow O_2^*$. An O_2 adsorbs at the O_{br} vacancy.

(iii) $O_2^* + CO^* \rightarrow OCOO$. The adsorbed O_2 reacts with the second adsorbed CO, forming an OCOO intermediate.

(iv) $OCOO \rightarrow CO_2 + O_{br}$. The OCOO intermediate dissociates into CO_2 and regenerates the catalyst.

We show in Fig. 3 the reaction free energy profiles for the best CO oxidation channel at 200 K and at 300 K, which occur at different Au particles, *i.e.* on $Au_{37}O_4$ at 200 K, and on $Au_{24}O_4$ at 300 K (both under 1 atm with CO 1% and O_2 21%). The reaction profiles at the two temperatures thus highlight the fact that the particle size matters for the activity: $Au_{24}O_4$ is more active at ambient temperature, while the close-packed particles as represented by $Au_{37}O_4$ are active only at extremely low temperatures (*i.e.* ~200 K). This is mainly because CO adsorption on $Au_{37}O_4$ is much weaker than that on $Au_{24}O_4$, leading to the temperature-dependence of the best reaction channel, as elaborated below. The gas phase free energy correction was made for CO and O_2 and the zero-point energy for all the surface states were taken into account in deriving the free energy profiles.

Taking CO oxidation on $Au_{24}O_4$ as an example, we illustrate how the reaction occurs. The most stable CO at the interfacial Au is at the Au site (Au* in Fig. 3) that is bonded with the lattice O_{br} (O_{br}^* in Fig. 3). Upon this adsorption, the Au atom moves outside along TiO_2 [001] by ~1 Å to maximally stabilize CO. The CO adsorption at this CO–Au–O_{br} configuration gains 1.10 eV in energy, and 0.46 eV in free energy (at 300 K and $p(CO) = 0.01$ atm). These results are consistent with the general knowledge that CO prefers to adsorb at the defective sites of Au and can reconstruct small Au particles. This adsorbed CO can react with its nearby O_{br} (next to the O_{br}^*) of the oxide to produce the first CO_2 with a barrier (E_b) of 0.57 eV (Fig. 3, TS1), in which the O_{br}–CO distance at the TS is 2.02 Å, which is quite typical for CO oxidation on metals. After the reaction, an O_v is created that is then filled by a gas-phase O_2 with the free adsorption energy of 0.42 eV. The adsorbed O_2 can react with a nearby adsorbed CO to form an OCOO complex by overcoming a low barrier of 0.31 eV (Fig. 3, TS2) and the reaction is exothermic by 0.32 eV. The dissociation of OCOO is also facile with a barrier of 0.34 eV (Fig. 3, TS3), after which a second CO_2 is released and the catalyst is recovered.

Compared to $Au_{24}O_4$, CO adsorption on $Au_{37}O_4$ is much weaker, which is due to the fact that the interfacial Au in $Au_{37}O_4$, (being close-packed) has a higher CN than that in $Au_{24}O_4$. Even at 200 K, CO adsorption on $Au_{37}O_4$ at the Au site analogous to that in $Au_{24}O_4$ is already endothermic by 0.12 eV for free energy (exothermic by 0.28 eV for energy). The weakly adsorbed CO can react with the nearby O_{br} with a very low barrier of only 0.13 eV. The subsequent OCOO formation becomes the rate-determining step with an overall free energy barrier of 0.52 eV (see Fig. 3).

To properly address the kinetics at different temperatures, we performed a microkinetic simulation for CO oxidation on the two catalysts using the free energetics derived from DFT and the results are shown in Fig. 4a. For the dome $Au_{24}O_4$ particle (red curve in Fig. 4a), the CO_2 production rate increases sharply from 0.29 mmol g_{Au}^{-1} s^{-1} at 220 K to a maximum of 45 mmol g_{Au}^{-1} s^{-1} at 300 K, then reduces to 28 mmol g_{Au}^{-1} s^{-1} at 350 K. For the $Au_{37}O_4$ catalyst (green in Fig. 4a), the activity grows slowly from 0.55 mmol g_{Au}^{-1} s^{-1} at 220 K to 1.1 mmol g_{Au}^{-1} s^{-1} at 350 K. Therefore, $Au_{24}O_4$ has a higher activity than $Au_{37}O_4$ above 230 K. Supported Au catalysts generally have a wide size distribution of Au particles, and so for simplicity, we considered a model catalyst that contains 10% $Au_{24}O_4$, 10% $Au_{37}O_4$ and 80% 2 nm Au particles and we evaluated its overall activity, as shown in the blue curve in Fig. 4a. Since Au particles larger than Au_{37} are close-packed and their activity at the interface is similar to that of Au_{37}, the activity of 2 nm Au can be deduced from $Au_{37}O_4$ as r_{37}/d^2 (where r_{37} is the rate of $Au_{37}O_4$ and d is the

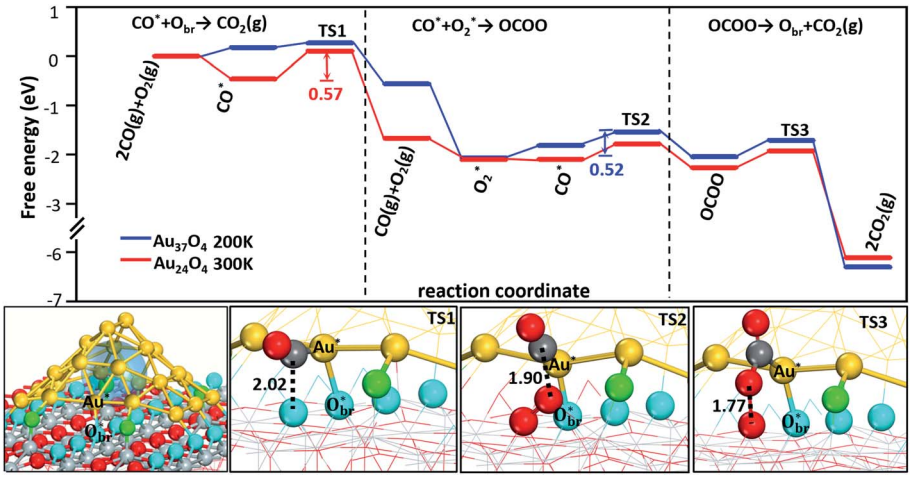

Fig. 3 Minimum free energy profiles for CO oxidation on $Au_{24}O_4/TiO_2$ at 300 K (red) and $Au_{37}O_4/TiO_2$ at 200 K (blue), both under 1 atm (CO 1%, O_2 21%). The snapshots of the three transition states (TS1, TS2 and TS3) on $Au_{24}O_4$ are shown in the lower panel, in which the key distances of the reactants are labelled with dotted lines. Au: yellow; C: gray; O in CO and O_2: red; O_{ad}: green; O_{br}: cyan.

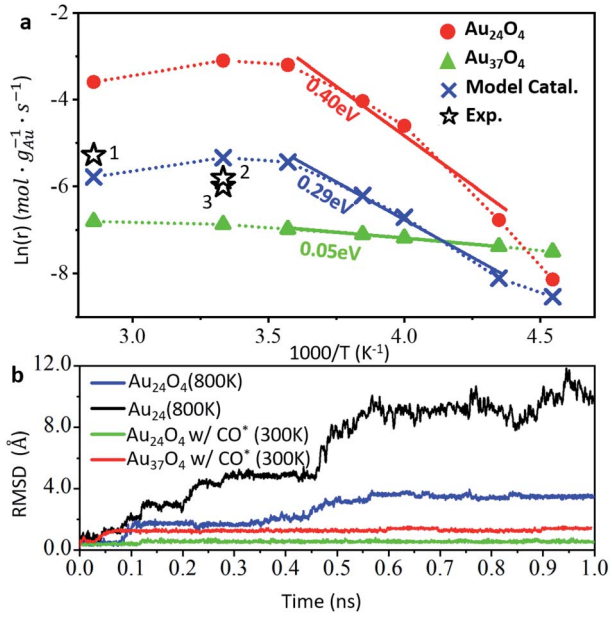

Fig. 4 Activity and stability of Au particles in CO oxidation. (a). Logarithm of CO_2 production rates *versus* the reciprocal of the temperatures. Red line: $Au_{24}O_4/TiO_2$; green line: $Au_{37}O_4/TiO_2$; blue line: model catalyst containing 10% Au_{24}, 10% Au_{37} and 80% Au_{2nm} particles. The hollow pentastars represent experimental results ((1) Wang *et al.*,[62] (2) Yan *et al.*,[63] (3) Shao *et al.*[64]). E_a denotes the linearly fitted theoretical apparent barrier at 230–280 K. (b). The plot of the RMSD of Au atoms for different $Au_{24}O_m$ and $Au_{37}O_4$ particles with (w/) or without CO adsorption taken from MD simulations over time at different temperatures.

diameter of the particle, *i.e.* 2 nm in this model). The overall rate as shown by the blue curve follows the same trend as that of $Au_{24}O_4$, reaching a maximum of 4.8 mmol g_{Au}^{-1} s^{-1} at 300 K and slightly reducing to 3.1 mmol g_{Au}^{-1} s^{-1} at 350 K.

It is of significance to compare our theoretical prediction with the available experiments that reported high CO oxidation activity. Although supported Au catalysts can be synthesized by different methods to control the size of small Au particles, we found that the agreement for the overall rate is satisfactory between our model catalyst and different experimental data (star symbols numbered from 1 to 3 in Fig. 4a). For example, a 1% Au/TiO_2 catalyst synthesized from a tetranuclear gold complex by Goodman and co-workers was reported to have a CO oxidation rate of 3 mmol g_{Au}^{-1} s^{-1} at 300 K.[63] By carefully controlling the size of the Au particles, Shao *et al.* synthesized a 2.2 nm Au/TiO_2 catalyst, which could catalyze CO oxidation at a rate of 2.5 mmol g_{Au}^{-1} s^{-1} at 300 K.[64] These data compare well with 4.8 mmol g_{Au}^{-1} s^{-1} for our model catalyst. At 353 K, Behm and co-workers reported a CO oxidation rate of 5 mmol g_{Au}^{-1} s^{-1}using a commercial Au/TiO_2 catalyst.,[62] which is only slightly larger than 3.1 mmol g_{Au}^{-1} s^{-1} predicted from theory.

In addition to the rate, it is possible to deduce the apparent barrier (E_a) from Arrhenius plots. As shown in Fig. 4a, the fitted E_a values for the temperature range 230 to 280 K are 0.40, 0.05 and 0.29 eV for $Au_{24}O_4$, $Au_{37}O_4$ and our model catalyst, respectively. In contrast to $Au_{24}O_4$ which has a high activity and high apparent barrier, $Au_{37}O_4$ has a low apparent barrier and low activity, which can be attributed to the low barrier to surface reactions on $Au_{37}O_4$ (temperature-independent) and the overall high free energy barrier due to the low CO adsorption ability. The experimental apparent barrier is generally ~0.3 eV below 300 K as measured at low conversion conditions, being consistent with our data.[63–66] Interestingly, by synthesizing a series of Au/TiO_2 catalysts with different methods and gold precursors, Goodman and co-workers observed that the supported Au catalyst with higher activity exhibited higher E_a.[63] The best catalyst with an average diameter of 3 nm had the apparent E_a of 0.38 eV; the worst catalyst with a diameter of 7.7 nm had an apparent E_a of 0.19 eV. Our explanation for this intriguing phenomenon is now straightforward: it is related to the concentration of very small gold particles that can adsorb CO strongly, such as $Au_{24}O_4$, for which the surface reaction of

adsorbed CO reacting with lattice O contributes to the apparent barrier.

3.4. Stability of Au particles under reaction conditions

Finally, we would like to provide insights into the thermodynamic stability of Au particles under reaction conditions, which is one of the key factors for supported Au catalysts. Molecular dynamics (MD) calculations were carried out to measure directly the thermal stability of supported Au particles in the presence of CO and O_2. Firstly, we took $Au_{24}O_4$ systems as the example and performed 1 ns MD simulations at 800 K as shown in Fig. 4b and also in ESI Fig. S5.† We found that the $Au_{24}O_4$ dome is basically unchanged with the root mean square displacement (RMSD, eqn (S5) in ESI†) of Au, converging to 0.35 nm per atom, where Au atoms only locally exchange between neighbours. For comparison, in the absence of O_{ad}, the bare Au_{24} on TiO_2 undergoes a dramatic structure deformation at 800 K with a RMSD that is three times larger than that of $Au_{24}O_4$. It transforms eventually from the dome to a close-packed stick-like structure with a G_f value of +0.21 eV (also see Fig. 1c), which suggests the sintering tendency of Au particles on TiO_2 in the absence of an O_2 atmosphere.

Then, we considered the effect of CO adsorption on the particle stability. For 3 CO molecules adsorbed on $Au_{24}O_4/TiO_2$, the 1 ns MD simulation at 300 K shows that the structure is immobile, with an RMSD of only 0.080 nm. A similar result was also obtained for $Au_{37}O_4/TiO_2$ with 5 CO adsorbed at the interfacial Au, where the RMSD is 0.16 nm. These results indicate that due to the presence of the anchoring O_{ad} at Au periphery site, which is less reactive than lattice O, the Au particles are stable under reaction condition.

Our MD simulations confirm the high stability of Au particles on O-rich TiO_2 surfaces during CO oxidation, demonstrating the key anchoring role of the O_{ad} at the interface. These O_{ad} are not active during CO oxidation, but act as structural stabilizers to immobilize the Au particles. These results explain the previous experimental findings. For example, scanning tunneling microscopy experiments have shown that small Au particles prefer to attach to O_{br} rows.[10,60] In an O_2 atmosphere the particles can be more stable, *e.g.* Au_7 survives up to 341 K.[11] At elevated temperatures, CO oxidation with O_{ad} (the barrier is ~1.0 eV from our calculations) occurs, which leads to the formation of bare Au particles, and the catalyst soon undergoes sintering due to the high mobility of bare Au particles on TiO_2, as shown in the black curve in Fig. 4b.

4. Conclusion

The extreme size sensitivity of supported Au catalysts revealed theoretically not only explains the critical thickness of Au particles on TiO_2 for CO oxidation, but also reveals the potential to boost the catalytic activity by finely controlling the Au particle size. For titania-supported Au catalysts, the smallest stable structure, the Au_{24} dome, is in fact the key component for catalyzing low temperature CO oxidation. The presence of oxidation conditions which introduce interfacial O atoms is the prerequisite for stabilizing such small Au particles. With the advent of ML-based global PES exploration, we believe that many more catalyst active sites can be resolved technically under reaction conditions, which should not only bring us new chemistry, but also pave the way towards the rational design of catalysts through the optimization of the active site structure and composition.

Author contributions

C. S. and Z.-P. L. conceived the project and contributed to the design of the calculations and analyses of the data. Y. P. carried out most of the calculations and wrote the draft of the paper. All the authors discussed the results and commented on the manuscripts.

Conflicts of interest

There are no conflicts to declare.

Acknowledgements

This work was supported by the National Key Research and Development Program of China (2018YFA0208600) and the National Science Foundation of China (91945301, 92061112, 21533001, 22033003, 91645201 and 91745201).

References

1 L. Liu and A. Corma, *Chem. Rev.*, 2018, **118**, 4981–5079.
2 Q. Fu, F. Yang and X. Bao, *Acc. Chem. Res.*, 2013, **46**, 1692–1701.
3 G. Ertl, *Angew. Chem., Int. Ed.*, 2008, **47**, 3524–3535.
4 R. Schlögl, *Angew. Chem., Int. Ed.*, 2015, **54**, 3465–3520.
5 T. W. van Deelen, C. Hernández Mejía and K. P. de Jong, *Nat. Catal.*, 2019, **2**, 955–970.
6 A. T. Bell, *Science*, 2003, **299**, 1688–1691.
7 R. Ciriminna, E. Falletta, C. Della Pina, J. H. Teles and M. Pagliaro, *Angew. Chem., Int. Ed.*, 2016, **55**, 14210–14217.
8 A. A. Herzing, C. J. Kiely, A. F. Carley, P. Landon and G. J. Hutchings, *Science*, 2008, **321**, 1331–1335.
9 A. Bruix, J. T. Margraf, M. Andersen and K. Reuter, *Nat. Catal.*, 2019, **2**, 659–670.
10 M. Valden, X. Lai and D. W. Goodman, *Science*, 1998, **281**, 1647–1650.
11 D. Matthey, J. G. Wang, S. Wendt, J. Matthiesen, R. Schaub, E. Lægsgaard, B. Hammer and F. Besenbacher, *Science*, 2007, **315**, 1692.
12 A. S. K. Hashmi and G. J. Hutchings, *Angew. Chem., Int. Ed.*, 2006, **45**, 7896–7936.
13 B. K. Min and C. M. Friend, *Chem. Rev.*, 2007, **107**, 2709–2724.
14 M. Haruta, *Catal. Today*, 1997, **36**, 153–166.
15 M. Haruta, S. Tsubota, T. Kobayashi, H. Kageyama, M. J. Genet and B. Delmon, *J. Catal.*, 1993, **144**, 175–192.
16 M. Haruta, N. Yamada, T. Kobayashi and S. Iijima, *J. Catal.*, 1989, **115**, 301–309.

17 M. Chen, Y. Cai, Z. Yan and D. W. Goodman, *J. Am. Chem. Soc.*, 2006, **128**, 6341–6346.
18 I. N. Remediakis, N. Lopez and J. K. Norskov, *Angew. Chem., Int. Ed.*, 2005, **44**, 1824–1826.
19 N. Lopez and J. K. Norskov, *J. Am. Chem. Soc.*, 2002, **124**, 11262–11263.
20 M. Haruta, *Gold Bull.*, 2004, **37**, 27–36.
21 G. C. Bond and D. T. Thompson, *Gold Bull.*, 2000, **33**, 41–51.
22 G. J. Hutchings, M. S. Hall, A. F. Carley, P. Landon, B. E. Solsona, C. J. Kiely, A. Herzing, M. Makkee, J. A. Moulijn, A. Overweg, J. C. Fierro-Gonzalez, J. Guzman and B. C. Gates, *J. Catal.*, 2006, **242**, 71–81.
23 J. Emmanuel, B. E. Hayden and J. Saleh-Subaie, *J. Catal.*, 2019, **369**, 175–180.
24 P. Mars and D. W. van Krevelen, *Chem. Eng. Sci.*, 1954, **3**, 41–59.
25 P. Schlexer, D. Widmann, R. J. Behm and G. Pacchioni, *ACS Catal.*, 2018, **8**, 6513–6525.
26 D. Widmann and R. J. Behm, *J. Catal.*, 2018, **357**, 263–273.
27 L. Li and X. C. Zeng, *J. Am. Chem. Soc.*, 2014, **136**, 15857–15860.
28 L. Li, Y. Gao, H. Li, Y. Zhao, Y. Pei, Z. Chen and X. C. Zeng, *J. Am. Chem. Soc.*, 2013, **135**, 19336–19346.
29 Y.-G. Wang, D. C. Cantu, M.-S. Lee, J. Li, V.-A. Glezakou and R. Rousseau, *J. Am. Chem. Soc.*, 2016, **138**, 10467–10476.
30 Y.-G. Wang, Y. Yoon, V.-A. Glezakou, J. Li and R. Rousseau, *J. Am. Chem. Soc.*, 2013, **135**, 10673–10683.
31 L. B. Vilhelmsen and B. Hammer, *ACS Catal.*, 2014, **4**, 1626–1631.
32 Z.-P. Liu, X.-Q. Gong, J. Kohanoff, C. Sanchez and P. Hu, *Phys. Rev. Lett.*, 2003, **91**, 266102.
33 Z. Duan and G. Henkelman, *ACS Catal.*, 2018, **8**, 1376–1383.
34 V. L. Deringer, M. A. Caro and G. Csányi, *Adv. Mater.*, 2019, **31**, 1902765.
35 K. T. Butler, D. W. Davies, H. Cartwright, O. Isayev and A. Walsh, *Nature*, 2018, **559**, 547–555.
36 H. Wang, Y. Ji and Y. Li, *Wiley Interdiscip. Rev.: Comput. Mol. Sci.*, 2020, **10**, e1421.
37 M. L. Paleico and J. Behler, *J. Chem. Phys.*, 2020, **153**, 054704.
38 J. Behler, *Angew. Chem., Int. Ed.*, 2017, **56**, 12828–12840.
39 J. Močkus, in *Optimization Techniques IFIP Technical Conference: Novosibirsk, July 1–7, 1974*, ed. G. I. Marchuk, Springer Berlin Heidelberg, Berlin, Heidelberg, 1975, pp. 400–404, DOI: 10.1007/978-3-662-38527-2_55.
40 C. Shang, X.-J. Zhang and Z.-P. Liu, *Phys. Chem. Chem. Phys.*, 2014, **16**, 17845–17856.
41 C. Shang and Z.-P. Liu, *J. Chem. Theory Comput.*, 2013, **9**, 1838–1845.
42 S.-D. Huang, C. Shang, P.-L. Kang and Z.-P. Liu, *Chem. Sci.*, 2018, **9**, 8644–8655.
43 S.-D. Huang, C. Shang, X.-J. Zhang and Z.-P. Liu, *Chem. Sci.*, 2017, **8**, 6327–6337.
44 S. Ma, C. Shang, C.-M. Wang and Z.-P. Liu, *Chem. Sci.*, 2020, **11**, 10113–10118.
45 S. Ma, S.-D. Huang and Z.-P. Liu, *Nat. Catal.*, 2019, **2**, 671–677.
46 P.-L. Kang, C. Shang and Z.-P. Liu, *J. Am. Chem. Soc.*, 2019, **141**, 20525–20536.
47 P.-L. Kang, C. Shang and Z.-P. Liu, *Acc. Chem. Res.*, 2020, **53**, 2119–2129.
48 S.-D. Huang, C. Shang, P.-L. Kang, X.-J. Zhang and Z.-P. Liu, *Wiley Interdiscip. Rev.: Comput. Mol. Sci.*, 2019, **9**, e1415.
49 S.-C. Ma, C. Shang and Z.-P. Liu, *J. Chem. Phys.*, 2019, **151**, 050901.
50 www.lasphub.com/supportings/AuTiCHO.pdf, accessed Feb. 22nd, 2021.
51 G. Kresse and D. Joubert, *Phys. Rev. B: Condens. Matter Mater. Phys.*, 1999, **59**, 1758–1775.
52 G. Kresse and J. Furthmüller, *Phys. Rev. B: Condens. Matter Mater. Phys.*, 1996, **54**, 11169–11186.
53 J. P. Perdew, K. Burke and M. Ernzerhof, *Phys. Rev. Lett.*, 1996, **77**, 3865–3868.
54 B. J. Morgan and G. W. Watson, *Surf. Sci.*, 2007, **601**, 5034–5041.
55 S. Grimme, J. Antony, S. Ehrlich and H. Krieg, *J. Chem. Phys.*, 2010, 132.
56 X.-J. Zhang, C. Shang and Z.-P. Liu, *J. Chem. Theory Comput.*, 2013, **9**, 5745–5753.
57 R. D. Lide, *CRC Handbook of Chemistry and Physics*, CRC press, 84th edn, 2003.
58 P. J. Steinhardt, D. R. Nelson and M. Ronchetti, *Phys. Rev. B: Condens. Matter Mater. Phys.*, 1983, **28**, 784–805.
59 X.-J. Zhang, C. Shang and Z.-P. Liu, *Phys. Chem. Chem. Phys.*, 2017, **19**, 4725–4733.
60 F. Cosandey and T. E. Madey, *Surf. Rev. Lett.*, 2001, **8**, 73–93.
61 Y. Maeda, M. Okumura, S. Tsubota, M. Kohyama and M. Haruta, *Appl. Surf. Sci.*, 2004, **222**, 409–414.
62 Y. Wang, D. Widmann and R. J. Behm, *ACS Catal.*, 2017, **7**, 2339–2345.
63 Z. Yan, S. Chinta, A. A. Mohamed, J. P. Fackler and D. W. Goodman, *Catal. Lett.*, 2006, **111**, 15–18.
64 B. Shao, J. Zhang, J. Huang, B. Qiao, Y. Su, S. Miao, Y. Zhou, D. Li, W. Huang and W. Shen, *Small Methods*, 2018, **2**, 1800273.
65 G. R. Bamwenda, S. K. Tsubota, T. Nakamura and M. M. Haruta, *Catal. Lett.*, 1997, **44**, 83–87.
66 Y. Tai, W. Yamaguchi, K. Tajiri and H. Kageyama, *Appl. Catal., A*, 2009, **364**, 143–149.